Achieving Superior Strength and Ductility Combination Through Cryorolling in 2219 Aluminum Alloy

K. Sivaprasad, B. Blessto ⓘ, V. Muthupandi, and M. Arumugam

In aluminum 2219 alloy, a combination of ultra-fine grains and coarse grains was established through cryorolling. Formation of bimodal grain distribution was confirmed using electron backscattered diffraction analysis, transmission electron microscopy and x-ray diffraction analysis. Cryorolled samples showed a 3% increase in strength, with a 4% increase in ductility. An increase in dislocation density, reduced slip distance and bimodal grain structure were attributed to the strength–ductility combination. Dislocation annihilation rate and driving force for dislocation movement were also determined based on the temperature of deformation and dislocation density in rolled material. The unidirectional and cross-directional cryorolled samples resulted in a grain size ranging from 510 nm to 73 μm and 340 nm to 42 μm, respectively.

1. Introduction

Ultra-fine grains (UFG) are produced either by sintering powders into alloy through deposition/ball milling or by introducing a high amount of dislocation density on a dense polycrystalline material through plastic deformation (Ref 1). Severe plastic deformation (SPD) processes are certain to increase the strength in room temperature and ductility at elevated temperatures (Ref 2). The ultra-fine-grained material tailored by these SPD processes was found to have applications in various severe environments. Though they provide a decent ductility at high temperatures, their plastic properties are inadequate in the working environment. A combination of high strength and ductility (Ref 3) in the material is very much desirable for industrial applications. For optimizing the expected mechanical properties, changes happening during recovery and recrystallization are notable (Ref 4-6). Several mechanisms like a combination of plastic deformation processes (Ref 7), activating micro-shear banding (Ref 8-10) and tailoring second phase particles in a fine-grained metal matrix (Ref 11) have been accustomed by researchers to achieve high strength and ductility. Cryorolling, one of the plastic deformation technique, is a research area of interest in recent years. This processing method offers improvement in mechanical properties for less applied strain by the formation of ultra-fine grains (UFG < 10 μm) (Ref 1, 7, 12). The development of a bimodal grain structure is an effective way of obtaining necessary combined properties. Tailoring bimodal structure has proved to yield a good combination of properties in AA6082 (Ref 13), Al 5083 (Ref 14), AA2024 (Ref 15), AA8090 (Ref 16), Titanium (Ref 17) and stainless steel (Ref 18). AA2219 Al alloy having θ" phase (Al_2Cu) in the Al matrix exhibits grain boundary strengthening during cryorolling. The ductility of the material can be improved by tailoring the microstructure. Hence, in the current research work, the strength and ductility of rolled sheets were correlated with the changes detected in the microstructure. The effect of the dislocation parameters (dislocation annihilation rate and driving force for dislocation movement) on mechanical properties was explored.

2. Experimental Procedure

AA2219 are typically heat-treatable alloys used in aerospace industries. Optical emission spectroscopy (OES) of the alloy revealed the presence of Al (93.717%), Cu (5.86%), Mn (0.304%), Si (0.053%), Ti (0.029%), Zn (0.027%), Fe (0.007%) and Mg (0.003%). AA2219 alloy plates in the T87 condition are cold rolled and cryorolled up to 75% reduction in both unidirection and cross direction. Plates of 12 mm thickness were polished after grinding its sharp edges. They were rolled in room temperature (cold-rolling) and subzero temperature (cryorolling) with a 0.2 mm reduction in each pass. Rolling in cross direction refers to turning the plate to 90° in each pass. The room temperature rolled samples are termed as RTR75U and RTR75C in unidirection (single direction) and cross direction, respectively. Similarly, the cryorolled samples are termed as LNR75U and LNR75C in unidirection and cross direction, respectively.

The mirror-polished surface of the sample after etching with Keller's reagent was observed with an optical microscope. An Olympus GX41 inverted metallurgical microscope was used to view the microstructures of the rolled plates. XRD analysis is performed on a Rigaku Ultima III instrument at a scan rate of 0.01 from 20° to 100° to determine the crystal structure and phases formed during rolling. The tensile tests were performed on the sub-size dog bone specimen. The samples were tested at

K. Sivaprasad, B. Blessto, and **V. Muthupandi**, Advanced Materials Processing Laboratory, Department of Metallurgical and Materials Engineering, National Institute of Technology, Tiruchirappalli 620015, India; and **M. Arumugam**, Liquid Propulsion Systems Centre, Thiruvananthapuram 695547, India. Contact e-mail: bblessto@gmail.com.

a strain rate of 5×10^{-4}/s as per the ASTM-E08-16 standard. Kocks–Mecking plots that describe the hardening behavior in the plastic zone were generated from the tensile results. The fractography for the tensile specimens was analyzed and recorded with a JEOL high-resolution SEM.

The sample for electron backscatter diffraction (EBSD) analysis is prepared initially by grinding, followed by grid polishing. Then, the sample is electro-polished to remove the surface irregularities. EBSD analysis was performed using an FEI Quanta 3D FEG-TSL^{TM} system at a step size of 0.1 μm for an area of 400 μm × 400 μm. The diffracted electrons from the emission gun form corresponding Kikuchi patterns, which predict the crystallographic orientation of the grains. The grains were reconstructed using orientational image mapping mode in TSL OIM image analyzer 8 software. The grain size of the rolled samples is determined from the quick grain size mapping with an absolute confidence index of 0.1. For transmission electron microscopy (TEM) analysis, the samples were reduced to 0.1 mm foil through a series of disk and emery polishing. Then a 3 mm slot was cut off from the thin foil using a disk punch. The specimen was mounted on a grinder wheel and its thickness was reduced further using a disk grinder. Then, the resulted thin foil is loaded in a Gatan precision ion polishing system (PIPS) having double penning ion guns of beam diameter 350 μm. The beam diameter was adjusted using argon gas and was ion milled till attaining electron transparency. The ion milling chamber was maintained in a vacuum of 8×10^{-6} Torr pressure. The TEM images of the ion milled samples were obtained using a JOEL JEM 2100 equipment at an accelerating voltage of 20 kV and a high magnification of 10,000×.

3. Results and Discussion

3.1 Microstructure

The micrographs of the AA2219 rolled alloy captured under an optical microscope are illustrated in Fig. 1. The rolled samples show a well-deformed microstructure, while the alloy in the T87 condition shows a clear equiaxed grain structure. The presence of cell structure is distinct in the RTR75C samples (Fig. 1c) when compared to the single direction rolled condition. The formation of the cell structure is due to higher strain accumulation as a result of a change in the strain path while rolling. A similar deformed cell structure was seen in large numbers in the cryorolled aluminum alloy at a 75 percent reduction in the works done by Joshi et al. and Shanmugasundaram et al. (Ref 19, 20). The presence of shear bands is evident from the micrographs of RTR75U and LNR75U samples. These microstructural features have a direct relation with the strength of the rolled alloy.

The ultra-fine grains formed in the rolled samples are studied by TEM analysis because of magnification restrictions in the optical microscope. The micrographs of LNR75U captured under high-resolution TEM in bright field mode are illustrated in Fig. 2. The LNR75U sample was accumulated by high dislocation density along with dislocation cell structures. A combination of ultra-fine grains and coarser grains in equal proportion was observed in the TEM micrograph. The size distribution of the grains was determined by EBSD analysis in later sections. The LNR75U material has a higher amount of high angle grain boundaries, which are evidenced by the fact

that low angle grain boundaries are unclear. The yellow diamond selected area electron diffraction (SAED) pattern shows continuous rings indicating a wide distribution of high misorientation angles among the UFGs. The yellow circle SAED spot pattern represents coarser grains at specific areas.

3.2 XRD Analysis

The XRD line profile analysis done on the base T87 as well as rolled alloy is shown in Fig. 3. The patterns show Al_2Cu peaks at ~ 43° and ~ 46°, proving that the mechanism of strengthening takes place by precipitates. The pattern says that there are no additional phases formed in the rolled material due to plastic deformation. The intensity of Al_2Cu peaks is weak in RTR75C and LNR75C samples due to the dissolution of precipitates into the Al matrix because of the Oswald ripening effect in the cross rolling route (Ref 21). Such effect was also seen in cryo milled Al7075 alloy where the $MgZn_2$ precipitates were dissolved into the Al matrix (Ref 22). Moreover, the cross-directional rolled alloy has a larger volume of grain boundaries, which bring about a low concentration of vacancies leading to lesser precipitate nucleation zones. Comparable results were obtained in work done by Hu et al. in Al7075 alloy (Ref 23). The patterns were further explored by Williamson–Hall analysis to determine the dislocation density and average grain size (d). The dislocation density was calculated as per the report by Ma and his co-workers (Ref 22).

3.3 Tensile and Work Hardening Behavior

The tensile properties are tabulated in Table 1 and the tensile graphs are plotted in Fig. 4(a). The samples rolled to a 75% reduction have exhibited higher strength than the alloy in the T87 condition. The enhanced strength is due to the pinning of dislocations (in order of 10^{15}) that leads to higher dislocation–dislocation interactions at higher strain (Ref 24). Among the samples rolled to 75% reduction, the LNR75U condition exhibits the highest strength due to a maximum dislocation density of 3.94×10^{15}. The yield strength of the LNR75U and LNR75C samples are almost the same, i.e., 456 MPa, which is far higher than the T87 base material. The RTR sheet for the single direction and cross-direction show the strength of 451 and 351 MPa, respectively. Meanwhile, the cryorolled sheet at 75% reduction shows an enhanced strength of ~ 2 and ~ 30% than RTR in single and cross directions. The enhancement in strength can be explained by the dislocation annihilation rate (6.13), which depends only on the low deformation temperature for cryorolling. Also, the LNR75U samples showed an increase of 3% strength and 4% ductility than RTR75U samples attributable to a 4.35×10^{-9} driving force for dislocation movement. These results indicate that cryorolling plays a vital role in modifying the age-hardening kinetics in the alloy (Ref 25). The Kocks Mecking plot was drawn between dσ/dε versus the flow stress $\sigma - \sigma_y$ (Ref 26). The work hardening behavior was interpreted from the Kocks Mecking plot for the rolled AA2219 alloy, which is shown in Fig. 4(b). The rolled samples show a gradual drop in the hardening rate from the flow stress of 5-40 MPa in the plastic deformation region. This explains the higher strength obtained by the rolled alloys compared to the alloy in the T87 condition. Comparable results were obtained by Mei et al., in Al-Mg-Si alloy (Ref 27). The work hardening rate is high for cryorolled samples (around 520 MPa) due to dislocation segregation at the grain boundaries, as experienced by Wang et al. (Ref 28). The RTR75C samples
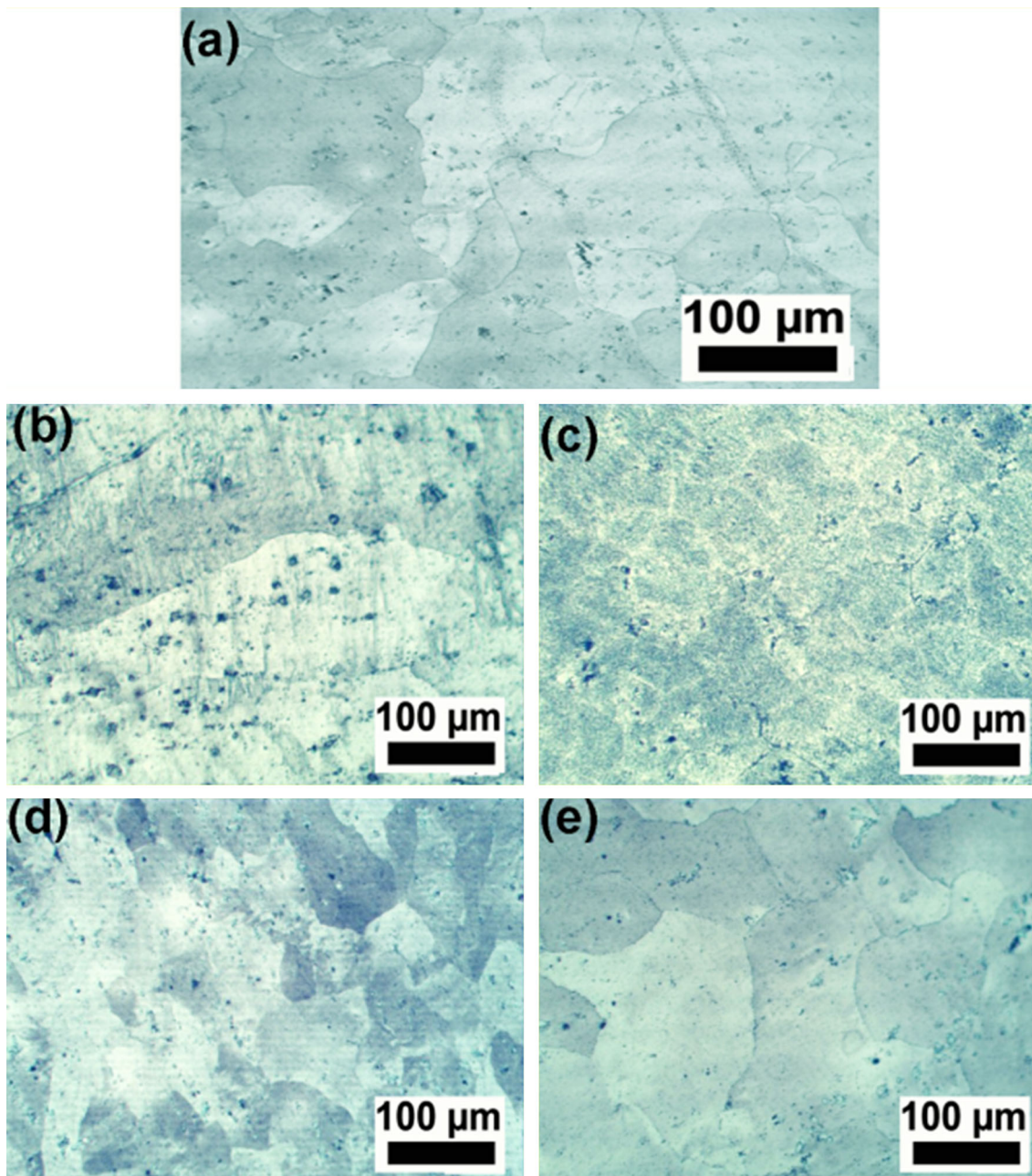
Fig. 1 Optical micrographs of (a) T87, (b) RTR75U, (c) RTR75C, (d) LNR75U, (e) LNR75C AA2219 samples

show reduced work hardening rate of 400 MPa followed by stage 3 falls till 270 MPa, which is the reason for its low yield strength of 351 MPa and high ductility of 12.4%.

The high ductility of the RTR75C sample is due to the cell structure and the high strength obtained in the unidirectional rolled sample is because of the shear banded structure, which is evident from the microstructural analysis. The ductility of each unidirectional rolled samples is $\sim$ 12%, which has increased to $\sim$ 13% in RTR75C and reduced to $\sim$ 11% in LNR75C. This attribute of cross rolled samples is accredited to the driving force for dislocation mobility, which is 9.05×10^{-9} for RTR75C and 3.28×10^{-9} for LNR75C. The reduced ductility of the cryorolled alloys is due to the inability of AA2219 material to strain harden at cryogenic temperature whose dislocation annihilation rate is as low as 6.13. It is evident that the ductility of the material

is directly proportional to a factor called dislocation annihilation rate, k (Ref 19, 29). The dislocation annihilation rate (Eq 1) and driving force for dislocation movement, P (Eq 2) (Ref 29) are factors that determine the strength and ductility combination of tensile properties of the material.

$$k = 1.334 \times 10^{-5}T^2 - 1.176 \times 10^{-3}T + 6.14 \qquad \text{(Eq 1)}$$

$$P = 0.5\rho Gb^2 \qquad \text{(Eq 2)}$$

where T is the deformation temperature, ρ is the amount of dislocation density, G is the shear modulus of AA2219 alloy and b is the burger vector.

The driving force present within the rolled alloy for grain boundary motion (P) is directly proportional to the amount of
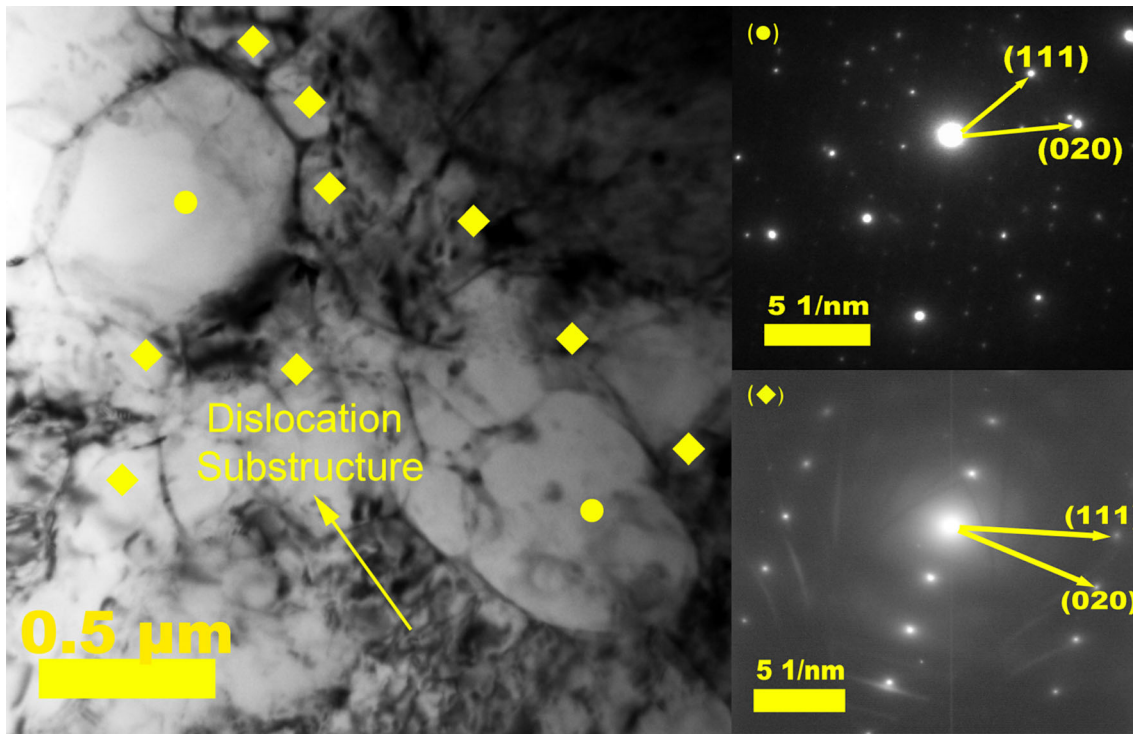
Fig. 2 A TEM micrograph with selected area diffraction pattern of LNR75U samples showing bimodal grain distribution. Yellow circle denotes coarser grains and yellow diamond denotes fine grains
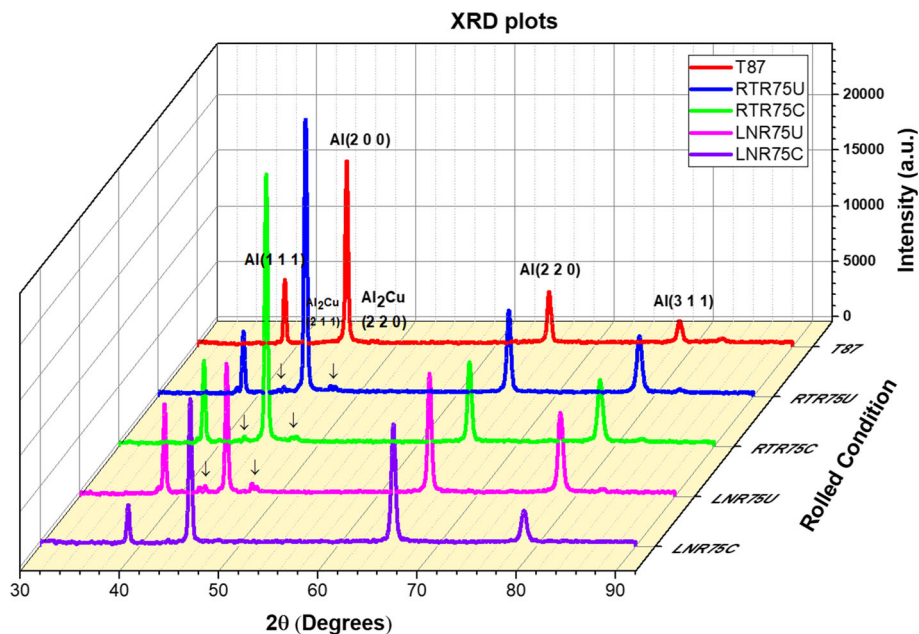
**Fig. 3** XRD patterns for base T87 and the rolled alloys

dislocation density. Deformation at subzero temperature has led to an increased number of dislocations, which is noticeable from Table 1. The alloy rolled at subzero temperature has developed higher dislocation quantity (3.94×10^{15}, 2.97×10^{15}), leading to finer grains than the RTR alloy. The dislocation annihilation rate parameter, k for RTR samples are higher (7.01), explaining the presence of lesser dislocation density (3.19×10^{15}, 2.27×10^{15}) at room temperature. Also, as the driving force for grain boundary motion increases, the

accumulated dislocations are free to move within the grain. It is well known that the dislocation movement increases the ductility of the material. Consequently, the elongation proves a direct relation with the driving force for grain boundary motion (P). This factor P further contributes to grain growth rate based on the mobility of the grain boundaries.

Equation 3 determine the relative slip distance λ (Ref 14), portraying the effect of deformation on the slip distance during tensile deformation.

Table 1 Mechanical properties of rolled AA2219 alloy

| Rolled condition	UTS, MPa	Yield, MPa	% elongation	Dislocation annihilation rate parameter, k	Driving force for GB movement, P	Dislocation density ρ, m^{-2}
T87	454 ± 10	388 ± 6	16.6 ± 0.4	...	...	...
RTR75U	501 ± 5	451 ± 3	11.3 ± 0.6	7.01	3.52×10^{-9}	3.19×10^{15}
RTR75C	456 ± 4	351 ± 3	12.4 ± 0.4	7.01	9.05×10^{-9}	2.27×10^{15}
LNR75U	513 ± 5	457 ± 4	11.7 ± 0.2	6.13	4.35×10^{-9}	3.94×10^{15}
LNR75C	489 ± 2	456 ± 5	10.5 ± 0.4	6.13	3.28×10^{-9}	2.97×10^{15}
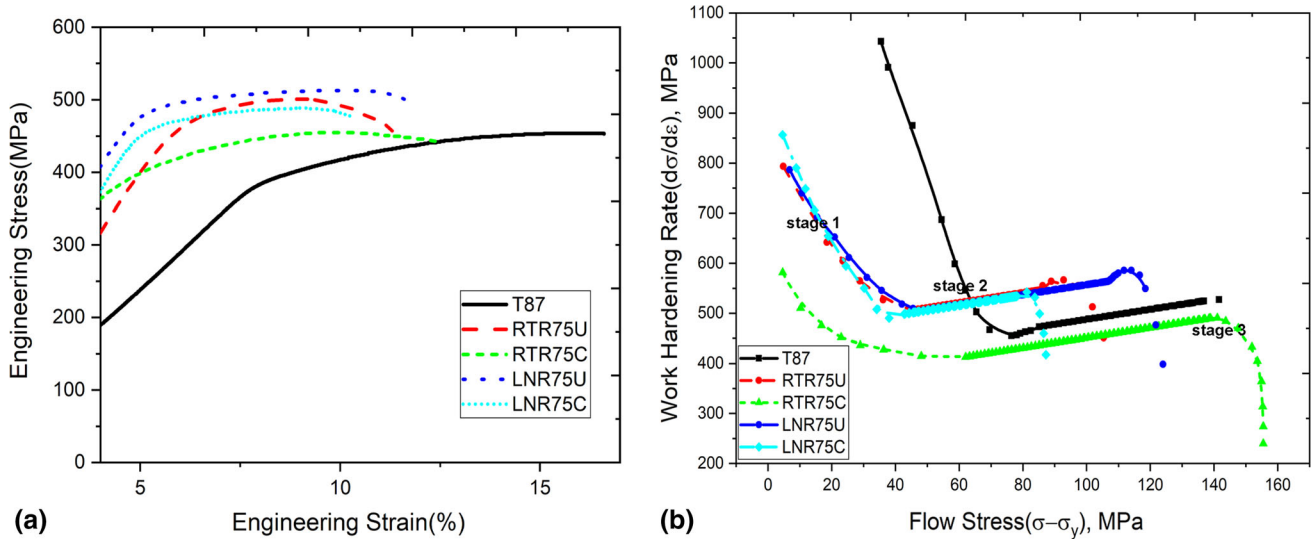
Fig. 4 (a) Tensile plot, (b) Kocks Mecking plot for rolled samples

$$\lambda = \left(\frac{b}{\varepsilon} \left(\frac{\sigma - \sigma_y}{\alpha G b} \right)^2 - \frac{1}{4d} \right)^{-1} \qquad \text{(Eq 3)}$$

In the above equation d is the average grain size determined from XRD analysis, ε is the true strain, α is a geometric factor and $\sigma - \sigma_y$ denotes the flow stress of the material. The slip distance plot is shown in Fig. 5 for all the rolled samples. The strain required to initiate the slip-dislocation movement is higher in the T87 sample (0.0068) rather than the other rolled alloys (ranges between 0.02 and 0.033). Slip planes are the region where the plastic deformation occurs effortlessly by dislocation movement. In FCC alloys, slip happens through {111} <110> closely packed plane. Moreover, the slip distance is observed lowest for LNR75U samples due to lesser slip-dislocation movement. The lower slip distance of 0.000134 mm explains the highest strength and reduced ductility in the LNR75U samples, while the slip distance of other rolled samples is greater than 0.0006 mm.

3.4 Fractography Analysis

The fractographic images of the rolled samples are shown in Fig. 6. The base alloy T87 shows the presence of dimples and intermetallic distributed along the fracture surface. Fine Al_2Cu intermetallic particle identified from XRD was found to be distributed homogeneously along the rolled alloy. Void coalescence, dimples and Al_2Cu intermetallic were found in the rolled samples. The nature of the intermetallics determines the
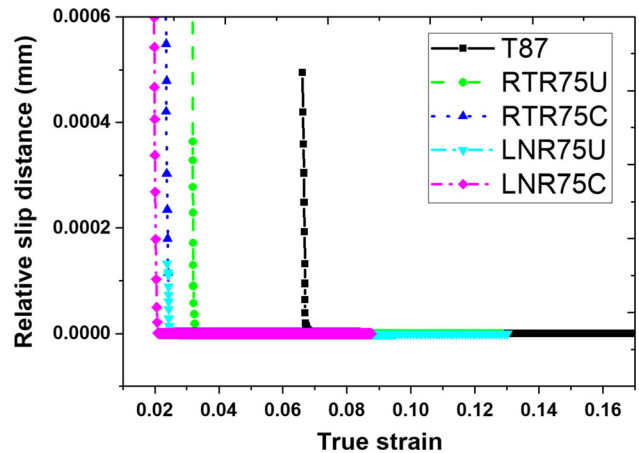
Fig. 5 Relative slip distance plot for rolled AA2219 alloy

formation of the void coalescence, dimples and the energy absorbed during fracture (Ref 30). The fracture surface of the rolled sample consists of voids and dimples with the plastic flow. The void coalescence is formed due to energy made up during deformation (Ref 31). The liquid nitrogen rolled samples show a larger void size due to lesser crystallite size as evident from the XRD analysis (Ref 16). The void present in RTR75C and LNR75C is lower than RTR75U and LNR75U because of the higher strain accumulated during the deformation process.

The failure of the material has taken place due to transgranular fracture along the grain boundaries and intermetallics. This has led to a de-cohesion from the matrix forming microvoids and dimples of variable sizes. The dimples were found to emerge from the intermetallics while the voids have nucleated grown and coalescence due to severe strain induced during deformation.

3.5 EBSD Analysis

The EBSD orientation image micrographs (OIMs) of the rolled samples performed along rolling versus normal direction is shown in Fig. 7. The alloy in the T87 condition was found to have equiaxed grains. The large fraction of unindexed regions present in the OIMs is due to finer crystallite size of the rolled alloy. More unindexed region in the cryorolled samples also confirms the finer crystallite size than the room temperature rolled alloy. Upon rolling, the distributed grains become fragmented and discontinuous along the rolling direction (Ref 13). Rolled samples show a significant change in its microstructure with elongated subgrains ensuring high misorientation angles. The RTR sample shows several elongated subgrains due to dynamic recovery phenomena. Since an adequate amount of stored energy is not available in the RTR samples, recrystallization has not happened. On the other hand, in cryorolled samples, the grains were further fragmented and a bimodal grain structure of coarse and ultra-fine grains were observed. The grain structure obtained is similar to the kind of bimodal arrangement observed by Xu et al. in AA6082 (Ref 13). Moreover, the inhomogeneous bimodal microstructure alleviates the tensile deformation by prompting strain hardening behavior, which is witnessed in Fig. 4(b).

The cross rolled sample shows different grain orientation in both the directions, while RTR samples show a single type of unrecrystallised subgrains in every direction. The suppression of dynamic recovery and cross-slip is the reason for the conservation of higher dislocation density in cryogenic rolled samples
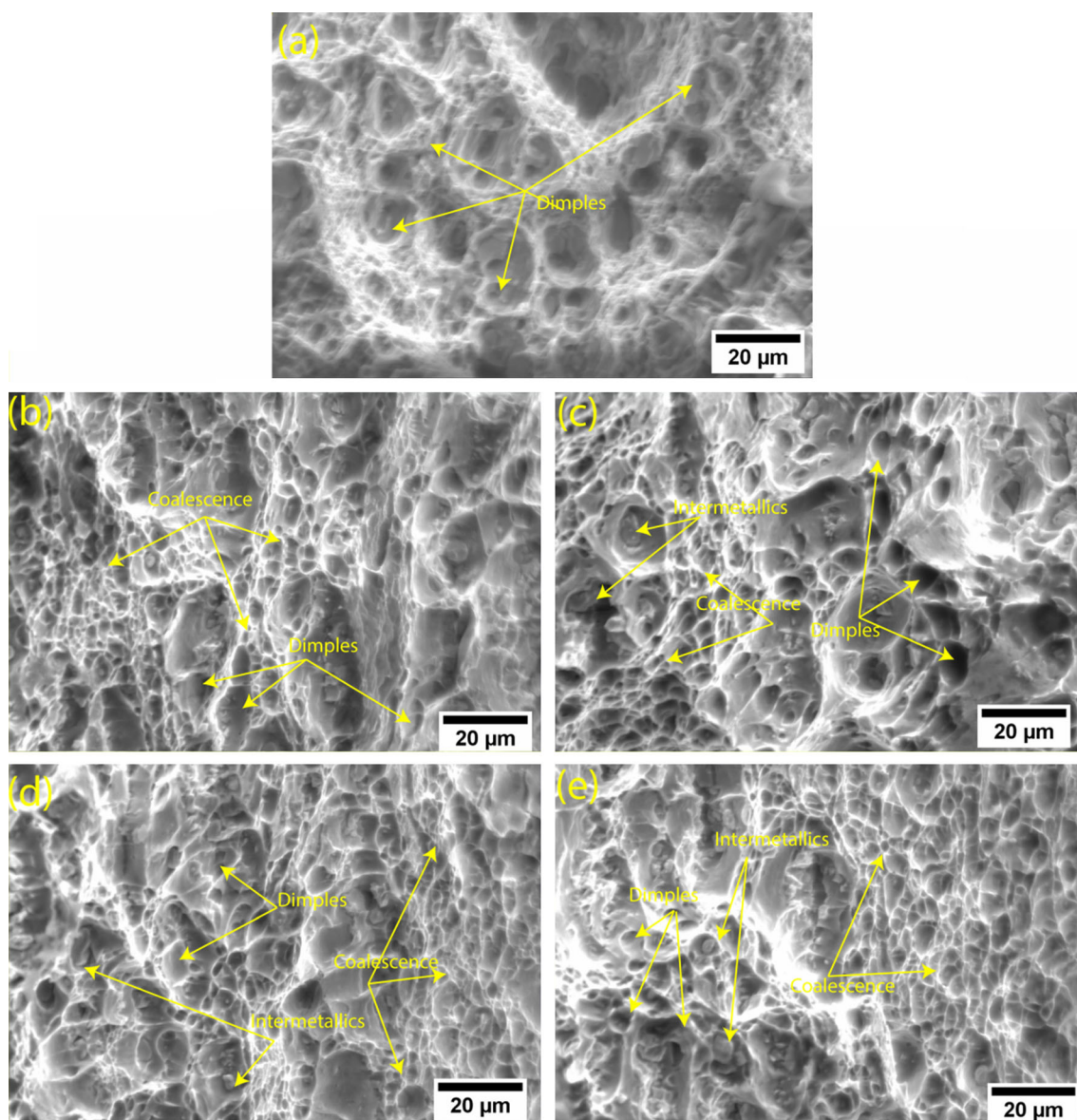
Fig. 6 Tensile fractography images of (a) T87, (b) RTR75U, (c) RTR75C, (d) LNR75U, (e) LNR75C

(Ref 14, 16, 32). The less dislocation annihilation rate parameter, the k value (6.13) ascertains the presence of enhanced dislocation. The higher dislocation density in cryorolled alloy had led to a higher strength than the RTR alloy which is evident from the tensile and XRD analysis. Bimodal size distribution was noted in the microstructural feature of LNR75U and LNR75C samples. The grain size distribution plot of the cryorolled samples is shown in Fig. 7 (f) and (g). The presence of a higher amount of ultra-fine grains (grain size of range 0.4-20 μm) and coarser grains (grain size ranging 70-75 μm in LNR75U and grain size ranging 40-45 μm in LNR75C) confirms the size inhomogeneity. The average grain size of the LNR75U (Fig. 7d) and LNR75C (Fig. 7e) samples are 32 and 22 μm, respectively. The bimodal grains are shown in the yellow square in Fig. 7(d) and (e), which are also witnessed from the TEM analysis shown in Fig. 2. The unidirectional and cross-directional cryorolled samples resulted in a bimodal grain distribution of size ranging from 510 nm to 73 μm and 340 nm to 42 μm, respectively. This bimodal grain development was the reason for improved ductility and strength in LNR75C sample. The formation of ultra-fine grains was the reason for enhanced strength in RTR75U and LNR75U samples.
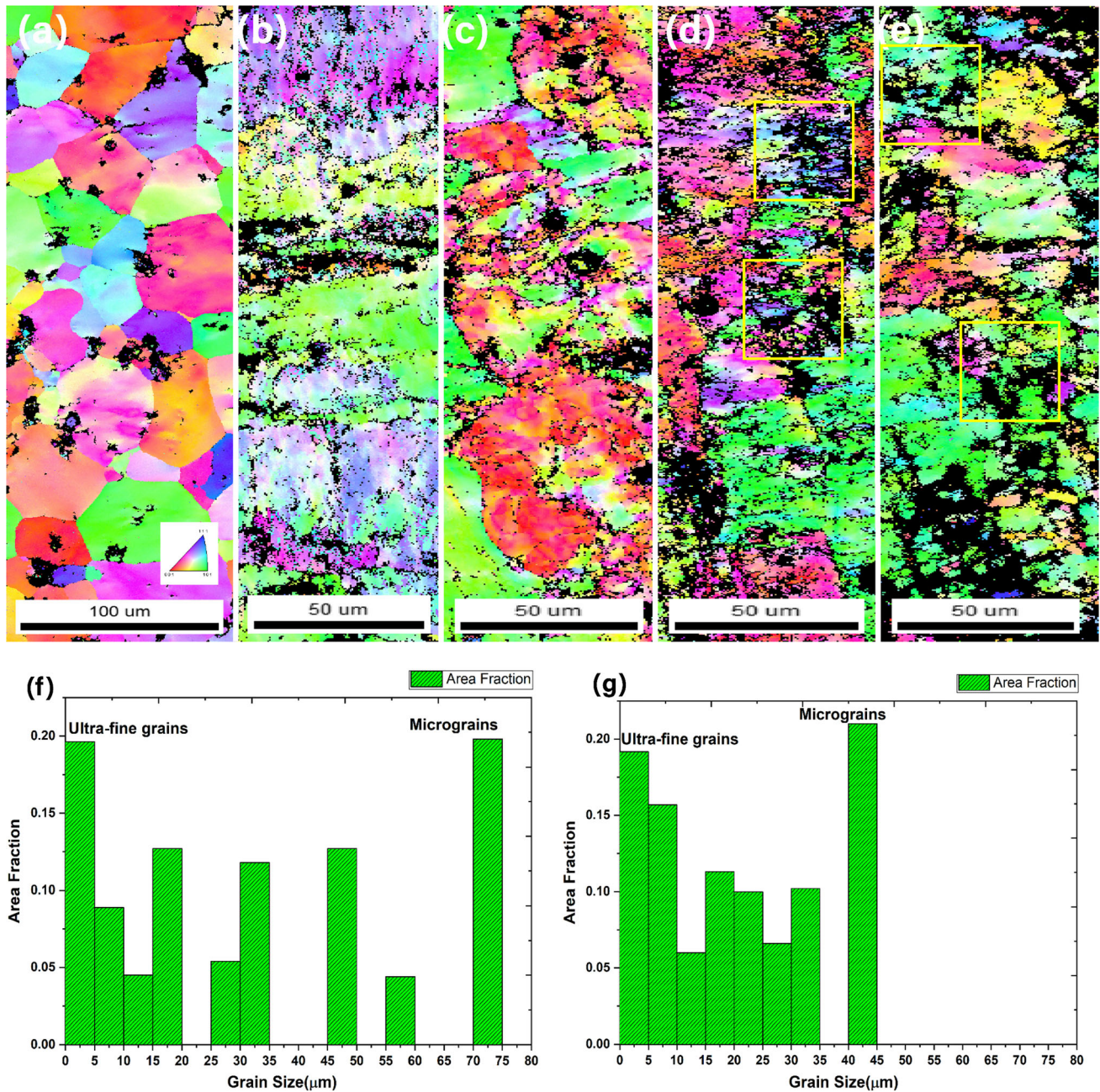
Fig. 7 Orientation image micrographs (OIMs) of AA2219 alloy: (a) T87 (inset: inverse pole figure), (b) RTR75U, (c) RTR75C, (d) LNR75U and (e) LNR75C; Histogram showing bimodal grain size distribution of (f) LNR75U, (g) LNR75C

4. Conclusion

AA2219 plates were rolled for a 75% reduction in the room temperature and cryogenic temperature with a view of obtaining combined strength and ductility. The rolled sample shows microstructure with well-deformed and unclear grain boundaries. Deformation cell structures were seen in the cross-directionally cryorolled sample. XRD analysis proves the presence of Al_2Cu precipitates and they were found to be dissolved in the matrix in cross rolled samples due to severe strain. The unidirectionally cryorolled material shows maximum strength of 513 MPa with 11.7% ductility due to suppression of dynamic recovery, cross-slip and formation of ultra-fine grains. The enhancement in strength is evident from the low relative slip distance of 0.000134 mm, leading to the pinning of dislocations and second phase particles. The dislocation annihilation rate and driving force for the dislocation movement play a substantial role in determining the material's mechanical property by affecting the dislocation density. The bimodal distribution of coarse and fine grains evident from the EBSD analysis of the cryorolled sample is responsible for its enhanced strength and ductility.

Acknowledgments

Data Availability Statement

The raw/processed data required to reproduce these findings cannot be shared at this time, but data will be made available on request.

References

1. Y. Huang and T.G. Langdon, Advances in Ultrafine-Grained Materials, *Mater. Today*, 2013, **16**(3), p 85–93. https://doi.org/10.1016/j.mattod.2013.03.004 (in English)
2. H. Yu, A.K. Tieu, C. Lu, X. Liu, M. Liu, A. Godbole, C. Kong, and Q. Qin, A New Insight Into Ductile Fracture of Ultrafine-Grained Al-Mg Alloys, *Sci. Rep.*, 2015, **5**, p 9568. https://doi.org/10.1038/srep09568 (in English)
3. E. Ma and J. Ding, Tailoring Structural Inhomogeneities in Metallic Glasses to Enable Tensile Ductility at Room Temperature, *Mater. Today*, 2016, **19**(10), p 568–579. https://doi.org/10.1016/j.mattod.2016.04.001 (in English)
4. O.V. Mishin, A. Godfrey, D. Juul Jensen, and N. Hansen, Recovery and Recrystallization in Commercial Purity Aluminum Cold Rolled to an Ultrahigh Strain, *Acta Mater.*, 2013, **61**(14), p 5354–5364. https://doi.org/10.1016/j.actamat.2013.05.024 (in English)
5. E.M. Lauridsen, H.F. Poulsen, S.F. Nielsen, and D. Juul Jensen, Recrystallization Kinetics of Individual Bulk Grains in 90% Cold-Rolled Aluminium, *Acta Mater.*, 2003, **51**(15), p 4423–4435. https://doi.org/10.1016/s1359-6454(03)00278-7 (in English)
6. B. Poorganji, P. Sepehrband, H. Jin, and S. Esmaeili, Effect of Cold Work and Non-isothermal Annealing on the Recrystallization Behavior and Texture Evolution of a Precipitation-Hardenable Aluminum Alloy, *Scripta Mater.*, 2010, **63**(12), p 1157–1160. https://doi.org/10.1016/j.scriptamat.2010.08.014 (in English)
7. Y. Estrin and A. Vinogradov, Extreme Grain Refinement by Severe Plastic Deformation: A Wealth of Challenging Science, *Acta Mater.*, 2013, **61**(3), p 782–817. https://doi.org/10.1016/j.actamat.2012.10.038 (in English)
8. I. Sabirov, Y. Estrin, M.R. Barnett, I. Timokhina, and P.D. Hodgson, Tensile Deformation of an Ultrafine-Grained Aluminium Alloy: Micro Shear Banding and Grain Boundary Sliding, *Acta Mater.*, 2008, **56**(10), p 2223–2230. https://doi.org/10.1016/j.actamat.2008.01.020 (in English)
9. I. Sabirov, M.R. Barnett, Y. Estrin, and P.D. Hodgson, The Effect of Strain Rate on the Deformation Mechanisms and the Strain Rate Sensitivity of an Ultra-Fine-Grained Al Alloy, *Scripta Mater.*, 2009, **61**(2), p 181–184. https://doi.org/10.1016/j.scriptamat.2009.03.032 (in English)
10. S. Malekjani, P.D. Hodgson, N.E. Stanford, and T.B. Hilditch, The Role of Shear Banding on the Fatigue Ductility of Ultrafine-Grained Aluminium, *Scripta Mater.*, 2013, **68**(5), p 269–272. https://doi.org/10.1016/j.scriptamat.2012.10.038 (in English)
11. A. Deschamps, F. De Geuser, Z. Horita, S. Lee, and G. Renou, Precipitation Kinetics in a Severely Plastically Deformed 7075 Aluminium Alloy, *Acta Mater.*, 2014, **66**, p 105–117. https://doi.org/10.1016/j.actamat.2013.11.071 (in English)
12. V. Subramanya Sarma, K. Sivaprasad, D. Sturm, and M. Heilmaier, Microstructure and Mechanical Properties of Ultra Fine Grained Cu-Zn and Cu-Al Alloys Produced by Cryorolling and Annealing, *Mater. Sci. Eng., A*, 2008, **489**(1), p 253–258. https://doi.org/10.1016/j.msea.2007.12.016 (in English)
13. Z. Xu, M. Liu, Z. Jia, and H.J. Roven, Effect of Cryorolling on Microstructure and Mechanical Properties of a Peak-Aged AA6082 Extrusion, *J. Alloys Compd.*, 2017, **695**, p 827–840. https://doi.org/10.1016/j.jallcom.2016.10.135 (in English)
14. K. Chandra Sekhar and R. Narayanasamy, Mechanical Properties and Formability of Cryorolled Commercial Pure Aluminium at Various Reductions, *Mater. Today Proc.*, 2018, **5**(2), p 6888–6896. https://doi.org/10.1016/j.matpr.2017.11.350 (in English)
15. D. Doppalapudi, P. Venkatachalam, S.R. Kumar, B. Ravisankar, and K. Jayashankar, Improving the Mechanical Properties of 2024 Al Alloy by Cryo Rolling, *Trans. Indian Inst. Met.*, 2010, **63**(1), p 31–34. https://doi.org/10.1007/s12666-010-0005-1 (in English)
16. K.S.V.B.R. Krishna, S. Vigneshwaran, K.C. Sekhar, S.S.R. Akella, K. Sivaprasad, R. Narayanasamy, and K. Venkateswarlu, Mechanical Behavior and Void Coalescence Analysis of Cryorolled AA8090 Alloy, *Int. J. Adv. Manuf. Technol.*, 2016, **93**(1–4), p 253–259. https://doi.org/10.1007/s00170-016-8863-2 (in English)
17. D.K. Yang, P.D. Hodgson, and C.E. Wen, Simultaneously Enhanced Strength and Ductility of Titanium via Multimodal Grain Structure, *Scripta Mater.*, 2010, **63**(9), p 941–944. https://doi.org/10.1016/j.scriptamat.2010.07.010 (in English)
18. B. Roy, R. Kumar, and J. Das, Effect of Cryorolling on the Microstructure and Tensile Properties of Bulk Nano-Austenitic Stainless Steel, *Mater. Sci. Eng., A*, 2015, **631**, p 241–247. https://doi.org/10.1016/j.msea.2015.02.050 (in English)
19. A. Joshi, K.K. Yogesha, and R. Jayaganthan, Influence of Cryorolling and Followed by Annealing on High Cycle Fatigue BEHAVIOR of ultrafine Grained Al 2014 Alloy, *Mater. Charact.*, 2017, **127**, p 253–271. https://doi.org/10.1016/j.matchar.2017.02.003 (in English)
20. T. Shanmugasundaram, B.S. Murty, and V. Subramanya Sarma, Development of ultrafine grained high strength Al–Cu alloy by cryorolling, *Scripta Mater.*, 2006, **54**(12), p 2013–2017. https://doi.org/10.1016/j.scriptamat.2006.03.012 (in English)
21. S.K. Panigrahi and R. Jayaganthan, A Study on the Mechanical Properties of Cryorolled Al-Mg-Si Alloy, *Mater. Sci. Eng., A*, 2008, **480**(1–2), p 299–305. https://doi.org/10.1016/j.msea.2007.07.024 (in English)
22. K. Ma, H. Wen, T. Hu, T.D. Topping, D. Isheim, D.N. Seidman, E.J. Lavernia, and J.M. Schoenung, Mechanical Behavior and Strengthening Mechanisms in Ultrafine Grain Precipitation-Strengthened Aluminum Alloy, *Acta Mater.*, 2014, **62**, p 141–155. https://doi.org/10.1016/j.actamat.2013.09.042 (in English)
23. T. Hu, K. Ma, T.D. Topping, J.M. Schoenung, and E.J. Lavernia, Precipitation Phenomena in an Ultrafine-Grained Al Alloy, *Acta Mater.*, 2013, **61**(6), p 2163–2178. https://doi.org/10.1016/j.actamat.2012.12.037 (in English)
24. Y. Xiong, T. He, H. Li, Y. Lu, F. Ren, and A.A. Volinsky, Annealing Effects on Microstructure and Mechanical Properties of Cryorolled Fe-25Cr-20Ni Steel, *Mater. Sci. Eng., A*, 2017, **703**, p 68–75. https://doi.org/10.1016/j.msea.2017.07.056 (in English)

25. K. Changela, H. Krishnaswamy, and R.K. Digavalli, Development of Combined Groove Pressing and Rolling to Produce Ultra-Fine Grained Al Alloys and Comparison with Cryorolling, *Mater. Sci. Eng., A*, 2019, **760**, p 7–18. https://doi.org/10.1016/j.msea.2019.05.088 (in English)

26. U.F. Kocks and H. Mecking, Physics and Phenomenology of Strain Hardening: the FCC Case, *Prog. Mater Sci.*, 2003, **48**(3), p 171–273. https://doi.org/10.1016/S0079-6425(02)00003-8 (in English)

27. L. Mei, X.P. Chen, G.J. Huang, and Q. Liu, Improvement of Mechanical Properties of a Cryorolled Al-Mg-Si Alloy Through Warm Rolling and Aging, *J. Alloys Compd.*, 2019, **777**, p 259–263. https://doi.org/10.1016/j.jallcom.2018.11.012 (in English)

28. Y.M. Wang and E. Ma, Three Strategies to Achieve Uniform Tensile Deformation in a Nanostructured Metal, *Acta Mater.*, 2004, **52**(6), p 1699–1709. https://doi.org/10.1016/j.actamat.2003.12.022 (in English)

29. H. Yu, C. Lu, K. Tieu, X. Liu, Y. Sun, Q. Yu, and C. Kong, Asymmetric Cryorolling for Fabrication of Nanostructural Aluminum Sheets, *Sci. Rep.*, 2012, **2**, p 772. https://doi.org/10.1038/srep00772 (in English)

30. K. Kamal Babu, K. Panneerselvam, P. Sathiya, A.N. Haq, S. Sundarrajan, P. Mastanaiah, and C.V. Srinivasa Murthy, Effects of Mechanical, Metallurgical and Corrosion Properties of Cryorolled AA2219-T87 Aluminium Alloy, *Mater. Today Proc.*, 2017, **4**, p 285–293. https://doi.org/10.1016/j.matpr.2017.01.023 (in English)

31. S. Vigneshwaran, K. Sivaprasad, R. Narayanasamy, and K. Venkateswarlu, Microstructure and Mechanical Properties of Al-3 Mg-0.25 Sc Alloy Sheets Produced by Cryorolling, *Mater. Sci. Eng., A*, 2019, **740–741**, p 49–62. https://doi.org/10.1016/j.msea.2018.10.044 (in English)

32. R. Jayaganthan, H.G. Brokmeier, B. Schwebke, and S.K. Panigrahi, Microstructure and Texture Evolution in Cryorolled Al 7075 Alloy, *J. Alloys Compd.*, 2010, **496**(1–2), p 183–188. https://doi.org/10.1016/j.jallcom.2010.02.111 (in English)